Lasers in Medical Science (2019) 34:1353–1363
https://doi.org/10.1007/s10103-019-02725-4

ORIGINAL ARTICLE

The photocytotoxicity effect of cationic sulfonated corrole towards lung cancer cells: in vitro and in vivo study

Zhao Zhang[1] · Hua-Jun Yu[1] · Hui Huang[1] · Bei Wan[2] · Shang Wu[1] · Hai-Yang Liu[2] · Hai-Tao Zhang[1]

Received: 25 September 2018 / Accepted: 15 January 2019 / Published online: 2 February 2019

Abstract

Corrole is a kind of new and promising photosensitizer (PS) in cancer photodynamic therapy (PDT). However, the protein molecular mechanism of PDT activity for corrole under light irradiation is still not clear. In this paper, water-soluble cationic sulfonated corrole (**1**) and its metal complexes (**1-Fe**, **1-Mn**, and **1-Cu**) were prepared, and the photodynamic anti-cancer activity against various tumor cells was investigated by MTT assay. The potential molecular mechanism of PDT activity was elucidated by fluorescence microscope, flow cytometry, molecular docking, and western blotting analysis. Besides, the potential PDT anti-tumor effect of **1** in vivo was assessed in human tumor xenografts in mice. Quantitative analysis revealed that **1**'s phototoxicity triggered a significant generation of reactive oxygen species, causing disruption of mitochondrial membrane potential. The results of western blotting (WB) assay shown in **1**'s phototoxicity could induce cell apoptosis via ROS-mediated mitochondrial caspase apoptosis pathway, in which SIRT1 protein degradation played a key role. PTD activity in vivo shown in **1** could significantly reduce the growth of A549 xenografted tumor, without obvious loss of mice body weight. We clearly found that cationic sulfonated corrole is a potential candidate of PS in vitro and in vivo. The phototoxicity of **1** could induce A549 cell apoptosis by inducing ROS production increase, further to activate the mitochondrial apoptosis pathway. We concluded that SIRT1 protein is a more appropriate target in this progress.

Keywords Corrole · Photocytotoxicity · ROS-mediated · SIRT1

Introduction

Corrole is a ring-contracted analogue of porphyrin [1, 2]. It had been extensively applicated in synthesis, catalysis, electrochemistry, and biological and medicinal studies [3–6]. In the last decade, corroles had proved the potential applications in various diseases [7–9], especially in cancer [10]. In 2003, corrole was firstly reported in cancer therapeutic, which could selectively damage MDA-MB-453 cancer cells [11]. The metallocorroles exhibited efficient cytostasis and cytotoxicity against SKMEL-28 cells by inducing late M phase arrest [12]. Besides, the cytotoxicity of doxorucibin against prostate cancer cell could improve threefold upon coadministration with corrole [12]. Whereafter, the functionalization of metallocorrole with carrier protein (HerGa) was prepared by Cross et al., which could enhance its cell permeability and showed a preferential accumulation in the tumors [13, 14]. The mechanistic study revealed that superoxide generation can be induced by HerGa under light, which leads to cytoskeletal and mitochondrial damage [15].

On the other hand, corrole also shows good results in PDT [4], due to their relatively intense absorption of long visible wavelengths and efficient singlet oxygen generation thereby [16]. In 2006, 10-(2-hydroxyphenyl)-5,15-bis(pentafluorophenyl) corrole inhibits nasophaaryngeal carcinoma cell (NPC) growth under light irradiation that was firstly reported by our group [17]. Later, the cytotoxicity of HerGa corrole was also found to be enhanced significantly under irradiation by augmenting mitochondrial disruption [18, 19]. 5,10,15-Tris(pentafluorophenyl)corrole

Zhao Zhang and Hua-Jun Yu contributed equally to this work.

✉ Hai-Yang Liu
chhyliu@scut.edu.cn

✉ Hai-Tao Zhang
taohaizhang33@163.com

[1] Department of Biochemistry and Molecular Biology, Guangdong Medical University, Zhanjiang 524023, People's Republic of China

[2] Department of Chemistry, Key Laboratory of Functional Molecular Engineering of Guangdong Province, South China University of Technology, Guangzhou 510640, People's Republic of China

conjugates with β-cyclodextrin moiety were found to be efficiently accumulated in lysosome and exhibit highly photosensitizing efficiency in HeLa cells [20]. In the last 2 years, we continuously reported two kinds of corroles in the PDT application: hydrophobic and hydrophilic [21–27]. Both of them showed a better PDT activity against A549, HeLa, and HepG2 cells. We found that the hydrophobic corrole can penetrate cell membranes in the absence of carrier proteins [22, 23, 25, 26]. Of the derivatives studied so far, gallium(III) corroles have been demonstrated as the most promising anti-cancer drugs [26]. Interestingly, the hydrophilic corrole had better PDT activity in cancer cells than the normal cells [27]. However, to our best knowledge, little information can be found on the cell protein mechanism of corrole's phototoxicity [26]. However, the mechanism study plays a key role in designing and developing new corroles [10, 15].

Inspired by these findings, and our continuous research of photodynamic activity of corrole [21–33], we here wish to report the proposed photocytoxicity signaling pathway of soluble cationic sulfonated corrole in cancer cells. The soluble cationic sulfonated corrole (**1**) and its iron (**1-Fe**), copper (**1-Cu**), and manganese (**1-Mn**) were prepared according to our early reports [29–33]. The photodynamic activity was measured by MTT assay. The potential molecular mechanism of PDT activity was estimated by fluorescence microscope, flow cytometry, molecular docking, and western blotting analysis (Scheme 1).

Experimental section

Materials

HepG2, HeLa, and A549 cell lines were purchased from American Type Culture Collection (ATCC, Manassas, VA). All aqueous solutions were deionized water. MTT, pancreatin, propidium iodide (PI), Dulbecco's modified eagle medium (DMEM), and bovine serum were purchased from Guangzhou Masscre Biological Technology Co., Ltd. (Guangzhou, China). JC-1 and DCFH-DA probe kits were purchased from Beyotime (Beijing, China). Muse™ Annexin V & Dead Cell Kit was obtained from Merck Millipore. Rabbit or antibody proteins PARP, P53, Bid, caspase-3, caspase-9, SIRT1, and GAPDH were purchased from Cell Signaling Technology, Inc. (BOC, USA). Irradiation was performed with a LED light (0127, Huayu Photoelectric Science & Technology Co. Ltd., China) with an emission peak at 625 nm and a bandwidth at half maximum (BWHM) of ± 15 nm. The intensity of light at the site of irradiation was 5 mW/cm^2, as measured with an M8 Spectrum Power Energy meter (San Diego, CA). And the irradiation time is 60 min for the in vitro test and 10 min for the in vivo test.

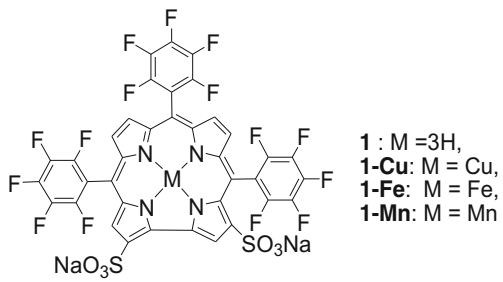

Scheme 1 The scheme of molecular structure of cationic sulfonated corrole and its metal complexes

In this paper, cationic sulfonated corrole and its metal complexes were prepared according to our previous study [29–33]. Briefly, a mixture of **1** and $Cu(OAc)_2$/$Mn(OAc)_2$/$FeCl_2$ was dissolved in 10 mL solvent (CH_3OH for **1-Cu**, DMF for **1-Mn**, pyridine for **1-Fe**) and re-fluxed for 30 min, followed by evaporation of the solvent. Metal corroles were obtained after the inorganic salts were separated by column chromatography on silica. The electronic spectrum of **1** in Tris–KCl buffer solution exhibits characteristic Soret band at 414 and 431 nm and the Q band at 589 and 619 nm, respectively. The MS spectrum of **1** exhibits a characteristic ion peak at *m*/*z* of 955.684 (100%), which is assigned to $[M\text{-}2Na + 2H]^-$. The electronic spectrum of **1-Fe** in Tris–KCl buffer solution exhibits characteristic Soret band at 404 nm and the Q band at 552 nm, respectively. The MS spectrum of **1-Fe** exhibits a characteristic ion peak at *m*/*z* of 503.492 (100%), which is assigned to $[(M\text{-}2Na)/2]^-$. The electronic spectrum of **1-Cu** in Tris–KCl buffer solution exhibits characteristic Soret band at 422 nm and the Q band at 537 and 583 nm, respectively. The MS spectrum of **1-Cu** exhibits a characteristic ion peak at *m*/*z* of 1160.826 (100%), which is assigned to $[M + H]^+$. The electronic spectrum of **1-Mn** in Tris–KCl buffer solution exhibits characteristic Soret band at 421 and 480 nm and the Q band at 578 and 644 nm, respectively. The MS spectrum of **1-Mn** exhibits a characteristic ion peak at *m*/*z* of 1007.934 (100%), which is assigned to $[M\text{-}2Na + 2H]^-$.

Cytotoxic activity assays

Cells were seeded in 96-well tissue culture plates (5×10^3 cells/well) for 24 h. The methods for the cytotoxicity, phototoxicity of corroles, and holographic imaging were described in our previous reports [27, 28].

Flow cytometry

A549 cells (1×10^6) were treated with **1** (1.25 and 2.5 μM) and illuminated as above described. The abbreviation of **1-L** and **1-D** mean **1** under light and in the dark, respectively, and the same below. Cells were rinsed with phosphate-buffered

solution (PBS) twice, fixed with 70% ethanol overnight. After rinsed with PBS, the cells were incubated with 5 μL PI (50 μg/mL) for 10 min in the dark, and the cells without PI had also been performed as a negative control. After rinsed with PBS, cells were analyzed by a flow cytometer (Muse Cell Analyzer, USA), and the percentage of cycle distribution cells was determined. A549 cells (1×10^6) were treated with **1** (1.25 and 2.5 μM) and illuminated as previously described. After 24 h, cells were dealt with dissociated; after rinsed with PBS, 100 μL cells were incubated with 100 μL Annexin V-7AAD double labeling in the dark. After 30 min, cells were analyzed by a flow cytometer (Muse Cell Analyzer, USA); the percentage of early and late phase of apoptosis cells was also determined.

ROS level detection

A549 cells (1×10^6) were treated with **1** and illuminated as our previous described [21, 26, 27]. Fluorescence intensity of DCFH-DA was determined by microplate analyzer (Varioskan Flash, Thermo, USA) with an excitation wavelength of 488 nm and emission at 525 nm. The fluorescence intensity is calculated by the determined fluorescence intensity minus the fluorescence intensity of **1** in the corresponding concentration.

Mitochondrial membrane potential assay

Mitochondrial membrane potential (MMP) was assayed by microplate analyzer (Varioskan Flash, Thermo, USA) using JC-1. Untreated and treated A549 cells were harvested and re-suspended in PBS; MMP was detected as described in our previous study [21, 26, 27]. The degree of damage was indicated by the percentage of the JC-1 monomer. The red and green fluorescent intensity was calculated by the florescent intensity minus the fluorescent intensity of **1** in the corresponding concentration.

Western blotting assay

The A549 cells were treated with cell lysis buffer (pH 8.0) that contained 50 mM Tris–HCl, 150 mM NaCl, 5 mM EDTA, 1% NP40, 0.05% PMSF, 2 mg/mL aprotinin, and 2 mg/mL leupeptin. Approximately 30 μg of protein/well was loaded for each sample. The detailed protocols refer to our previous publications [26, 34, 35].

Animals and implantation of cancer cells

The implantation of cancer cells was performed according to our previous report [26]. Female BALB/c nude mice (6 weeks old) were purchased and housed at Guangdong Medical College Laboratory Animal Center (Zhanjiang, China). Animal experiments were performed in accordance with protocols approved by the institutional ethics committee of Guangdong Medical College (Zhanjiang, China). The volume of the tumor mass was measured using an electronic caliper and calculated as (length × width^2) / 2 in mm^3. In the A549 xenograft studies, when the size of a tumor reached about 100 mm^3, the xenograft tumor-bearing nude mice were randomly placed into six groups: (1) the vehicle-treated group in the dark, (2) 0.5 mg/kg **1**-treated group in the dark, (3) 1.0 mg/kg **1**-treated group in the dark, (4) the light-treated alone group, (5) 0.5 mg/kg **1**-treated group in light, and (6) 1.0 mg/kg **1**-treated group in light using three mice per group. Ten microliters of corrole **1** was directly injected into the tumor mass of groups 2, 3, 5, and 6, respectively. After drug treatment, laser treatment was performed immediately. A second dose of the PDT treatment described above was repeated 2 days after the first dose. At the end of the observation period, the animals were euthanized by cervical dislocation.

Molecular docking analysis

Molecular docking was performed by using AutoDock 4.2 program. The crystal structure of SIRT1 (PDB ID 4ZZJ) was downloaded from the protein data bank. The molecular structure of SIRT1 and **1** for the docking simulation was edited by using AutoDockTools program. Cluster analysis was performed on the results of docking by using a root mean square (RMS) tolerance of 2.0 Å. The conformation with the lowest binding energy of the most populated cluster was picked out for further analysis. Molecular graphics and analyses were performed with the UCSF Chimera package [27].

Statistical analysis

Data are presented as the means ± standard error of the mean (SEM) from at least three independent experiments. Besides, data are presented as the mean ± standard error of the mean, $n = 3$. Statistical analysis was performed using one-way analysis of variance (ANOVA) followed by a Bonferroni post hoc for multiple group comparison or Student's unpaired t test for two-group comparison where appropriate. The analyses were performed using GraphPad Prism software version 6.0 (GraphPad Inc., La Jolla, CA, USA).

Results

Cytotoxic and phototoxic activities

The PDT effects of **1**, **1-Mn**, **1-Fe**, and **1-Cu** on A549, HeLa, and HepG2 cells were evaluated by MTT assay. After illumination, the viability of post-PDT cultures was determined the next day, and dose–response curves were obtained (Fig. 1a).

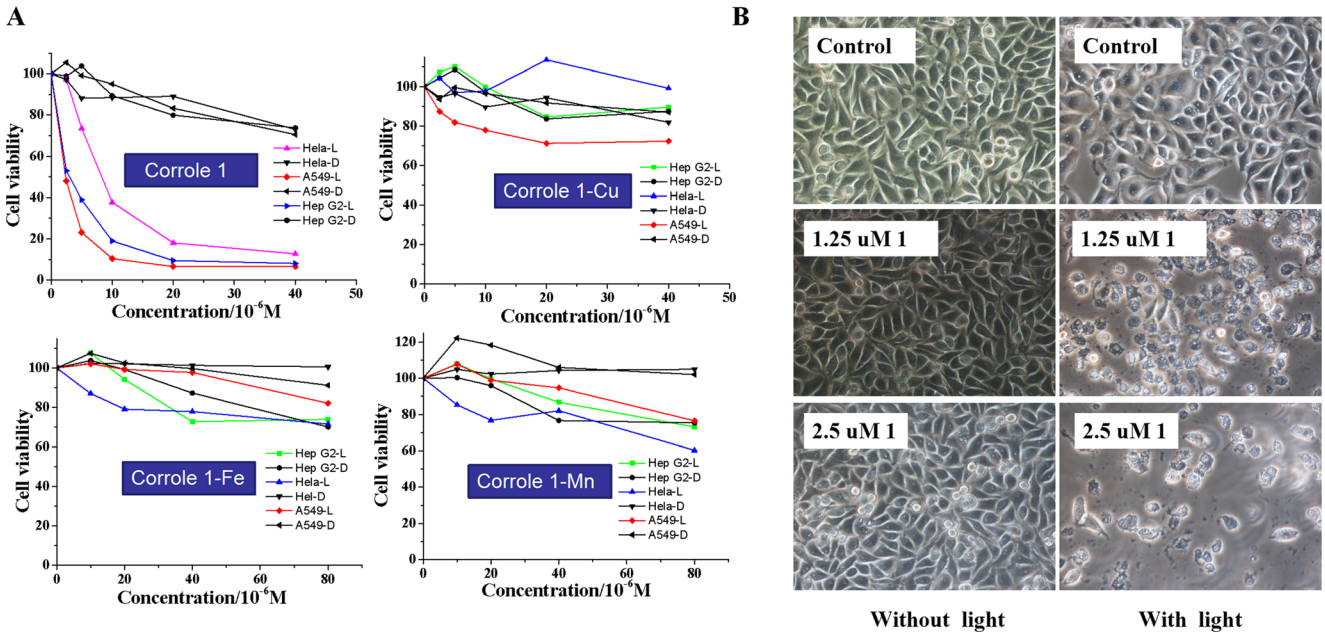

Fig. 1 Cytotoxic effects of **1**, **1-Cu**, **1-Fe**, and **1-Mn** on human cancer cells with/without illumination. **a** Dose–response curves for a 24-h exposure of human tumor cell lines, lung carcinoma (A549), hepatocellular cancer (HepG2), and cervical cancer (HeLa). The viabilities of each corrole-treated cell line are expressed as a percentage of untreated control growth. A sigmoidal dose–response curve was fitted to the data. **b** The optical images of A549 cells after incubation with/without **1** for 24 h

Cells incubated with corroles without illumination (dark control) were also kept in parallel. The results showed that the phototoxicity of corrole does not depend on the type of tumor cell lines and the central metals in this study. Considering that the gallium derivative corrole showed better PDT activity [18, 23, 25, 26], we can find that the phototoxicity of corrole depends on the central metals largely. Besides, the PDT activity IC50 value of corrole **1** on A549 cells was (calculated for the dose–response curve) 5.0 μM. Figure 1b shows the optical images of A549 cells upon treatment with **1**.

Induced A549 cell apoptotic though triggering generation of ROS causing disruption of MMP

To further understand the underlying mechanisms of **1** photocytotoxicity against A549 cell, HoloMonitor™ M3 and flow cytometric analysis were carried out. In this study, holographic and phase contrast images were recorded from the A549 cells after treatment with irradiation alone or combination with **1**. As shown in Fig. 2a, there was no significant change in 3D morphology of A549 cells after only receiving irradiation. However, after coadministration with **1**, the apoptotic cells were found (incubation 1 h). With the increasing of incubation time (no further illumination), the average cell volume decreased significantly.

Figure 3a shows the DNA content frequency histograms of A549 cell after treatment with **1**. Cells received **1**, and light showed a clear increasing of sub-G0/G1 peak, which is evidence for the occurrence of apoptosis in the cells [36]. Besides, cells after treatment with **1** and light also caused an increase of the G2/M phase population comparing to control sample.

In addition, Annexin V-7AAD double labeling was also used to detect cells' phosphatidylserine externalization, a hallmark of the early phase of apoptosis (Fig. 3b).

As shown in Fig. 4a, the change of MMP was detected. The reduction of values suggested that **1** induced the decrease of MMP and caused mitochondrial dysfunction. To determine whether **1** induces cell apoptosis and mitochondrial dysfunction through ROS, we evaluated the intracellular ROS generation in A549 cells (Fig. 4b). Altogether, these results indicated that **1** PDT activity induced apoptosis through the mitochondrial pathway via inducing ROS production in A549 cells.

Effect of 1 on apoptosis-related protein expression

The expression of apoptosis-related proteins in A549 cells after **1** PDT treatment was measured by western blotting assay (Fig. 5).

As shown in Fig. 5, after receiving **1** under illumination, the cleavage PARP (89 kb) appeared in A549 cells. We also find the increase expression of p53. The level of Bid was decreased; the activities of caspase-9 and caspase-3 were significantly enhanced, as indicated by their cleavage, as well as by the cleavage of PARP [26]. Moreover, as shown in Fig. 6, the expression level of anti-apoptotic protein SIRT1 was downregulated significantly.

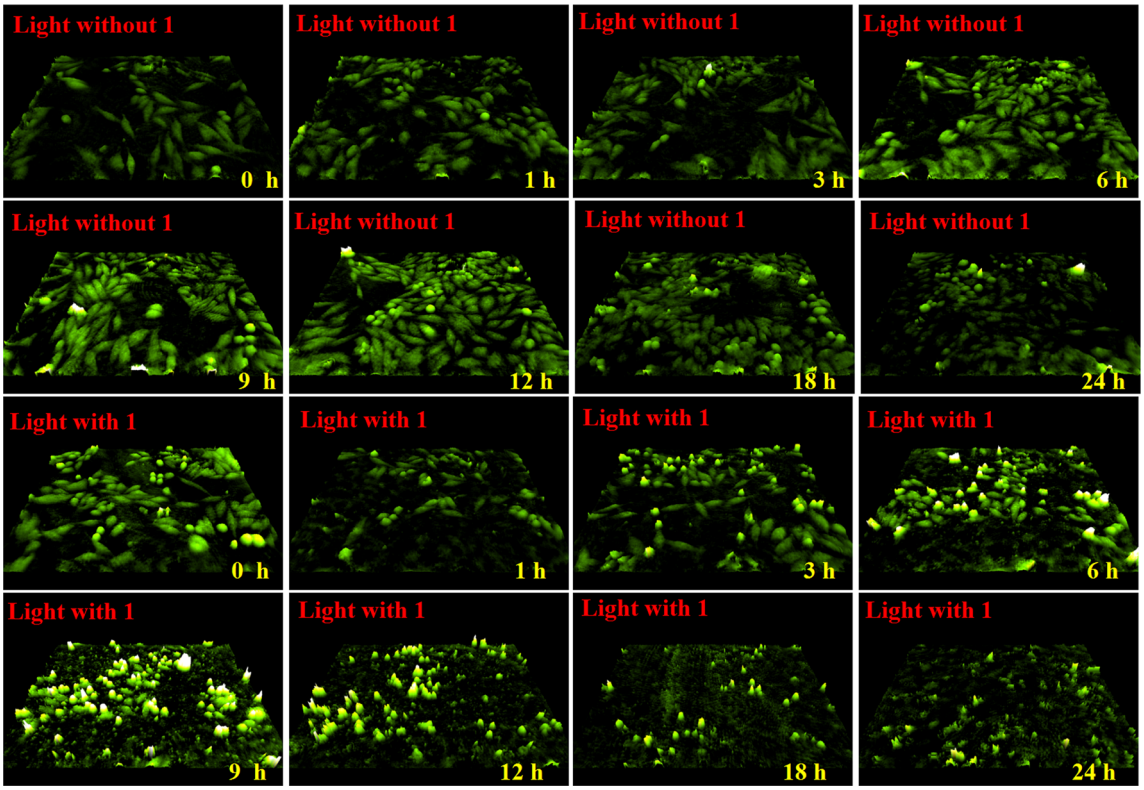

Fig. 2 Representative images of morphology of A549 cells treated with/without **1** under irradiation in 3D by HoloMonitor™ M3 (×200). Holographic imaging A549 cells were firstly seeded (2×10^5/well) on a 6-well plate the day before chemical treatment, then treated with **1** and illuminated as previously described (with 1 h). And then, the images were recorded immediately with HoloMonitor™ M3 once an hour

Furthermore, molecular docking simulation was carried out to investigate the binding behavior of **1** and SIRT1 protein. As shown in Fig. 7, the binding mode and sites were simulated. **1** can bind in the surface of SIRT1 protein by π–π stacking and hydrogen bond. The calculated binding energy of SIRT1 protein is − 8.79 kcal mol.

Anti-tumor effect of 1 in a xenograft model in vivo

The potential PDT anti-tumor effect of **1** in vivo was assessed in human tumor xenografts in mice. A549 cells were subcutaneously injected of A549 cells into the right armpit of the mice, and the results for the entire period of observation are displayed in Fig. 8.

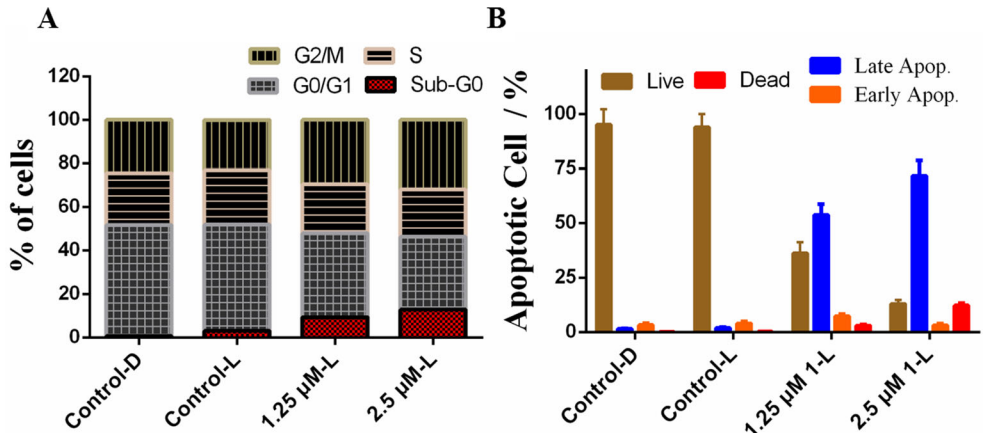

Fig. 3 **a** Cell cycle distribution of A549 cells. Cells were treated with **1** (0, 1.25, 2.5 μM) for 24 h with/without illumination by flow cytometry. The cells were immediately fixated at 0 °C with ethanol and then stained with PI; the DNA contents of each cell phase were analyzed by flow cytometry. **b** **1** induced A549 cell apoptosis. Cells were treated with **1** (0, 1.25, 2.5 μM) for 24 h with/without illumination; then, the cells were collected and analyzed by flow cytometry after being stained by Annexin V-PE and 7-AAD. The abbreviation of **1-L** means **1** under light; the abbreviation of **1-D** means **1** in the dark

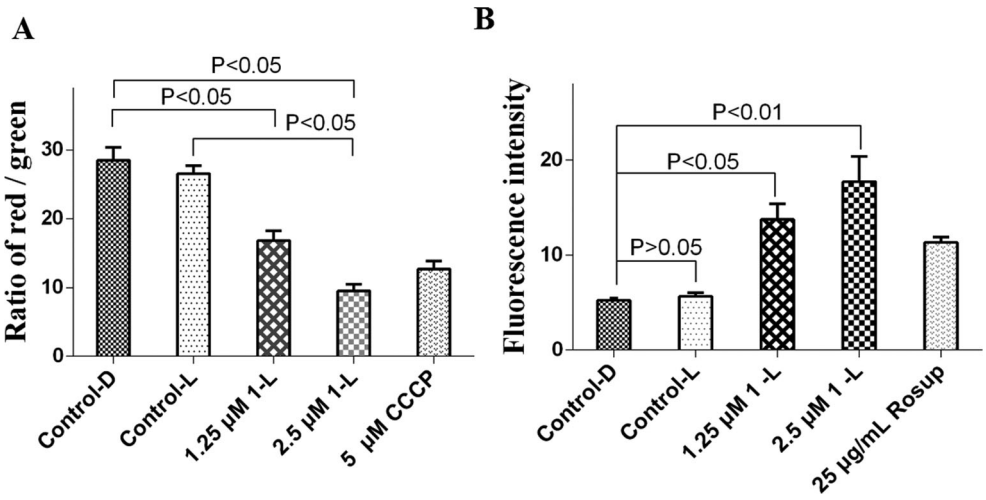

Fig. 4 **a** Effect of **1** on MMP decrease in A549 cells. **b** Intracellular ROS detection in A549 cells. $^{*}P < 0.05$; $^{\#}P < 0.05$; $^{**}P < 0.01$, significantly different compared with the control by *t* test, $n = 3$. The abbreviation of **1-L** means **1** under light; the abbreviation of **1-D** means **1** in the dark

Compared with the control group, **1**'s phototoxicity caused a significant suppression in tumor growth. The average weight of tumors in control group is 2.296 g. After being treated with 0.5 and 1.0 mg/kg of **1**, PDT treatment group is 1.1153 and 0.3727 g (Fig. 8b), respectively. Compared with the control vehicle group, neither 0.5 nor 1.0 mg/kg **1** caused no obvious loss of mice body weight (Fig. 8c), which indicated that **1**'s phototoxicity displayed no signs of toxicity in these mice.

Discussion

Photodynamic therapy is an effective clinical therapeutic method for a variety of solid tumors and non-malignant lesions [36–38], which has several advantages over other traditional therapies. For example, PDT is more controllable and selective though light irradiation [36]. Severe shortcomings of the first clinical PS have stimulated intensive research interest in the development ideal PS [39]. Hence, more and more efforts have been devoted to get new porphyrins and their derivatives in recent years [40–42]. As a kind of promising PS, corrole also shows a good result in PDT treatment [19–27].

The cytotoxicity and phototoxicity of **1**, **1-Mn**, **1-Fe**, and **1-Cu** against A549, HeLa, and HepG2 cells were evaluated by MTT assay. As shown in Fig. 1a, all the test cells are resistant to the corrole treatment without irradiation in the experiment condition. However, the phototoxicity of **1** increased sharply in all the test cell lines, especially in A549 cells. The enhanced photocytotoxicity relative to the dark control is an essential property for a photochemotherapeutic agent [27]. Besides, the metal corroles in this study showed little photocytotoxicity in the test cell lines. Considering that the gallium derivative corrole showed better PDT activity [18, 23, 25, 26], we can find that the phototoxicity of corrole depends on the central metals largely (which may be the result of paramagnetic effect).

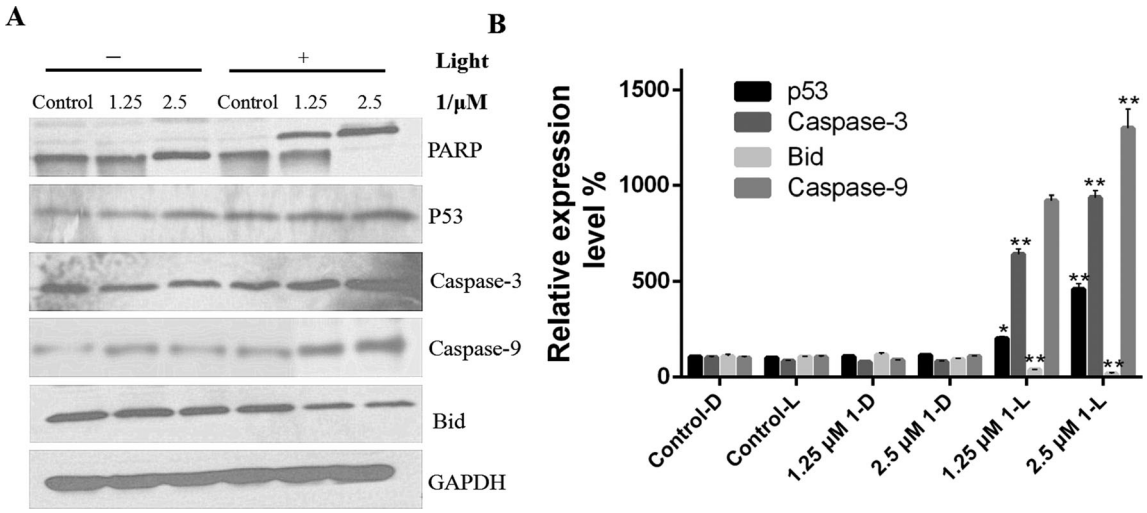

Fig. 5 The effect of **1** photocytotoxicity on apoptosis-related proteins involved in mitochondria caspase-dependent signaling pathway in A549 cells. The abbreviation of **1-L** means **1** under light; the abbreviation of **1-D** means **1** in the dark

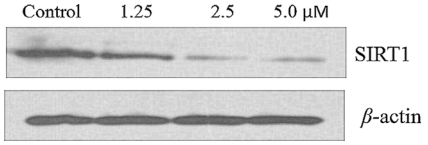

Fig. 6 Expression of SIRT1 in A549 cells after treatment with **1** under irradiation

Apoptosis and cycle arrest, or a combination of the two, can result in growth inhibition or cell death [43]. To further study the underlying mechanism of **1** photocytotoxicity, HoloMonitor™ M3 and flow cytometric analysis were carried out. The integrated image analysis of holographic microscopy algorithm could measure various cell parameters (including cell volume, cell thickness, cell shape convexity), which could reflect the cytotoxicity of drug [44]. During apoptosis, cell membrane permeability increases, and the optical density of cells decreases. In this study, holographic and phase contrast images were recorded. As shown in Fig. 2, there was no significant change after only receiving irradiation in 3D morphology of A549 cells. However, by coadministration with **1**, the apoptotic cells appeared in 1 h. The cells contracted; the area decreased, and the thickness increased. With the increase of time, the dead cells became very thin and large before it broke down into apoptosis bodies. After 24 h, the average volume of cells decreased significantly.

Here, the quantitative analysis of apoptosis was conducted by evaluating the percentage of sub-G0-G1 peak after labeling with PI. Figure 3a shows the DNA content frequency histograms of A549 cell after treatment with **1**. Cells received **1**, and light showed a clear increasing of sub-G0/G1 peak, which is an evidence for the occurrence of apoptosis [27]. Besides, A549 cells received **1**, and light also caused an increase of the G2/M phase population comparing to control sample. In addition, Annexin V-7AAD double labeling was also used to detect apoptosis rate. The basal late apoptotic population in the untreated and treated only light groups was less than 1.5%, which increased to 57.5% at 1.25 μM **1** and 74.6% at 2.5 μM **1** under illumination (Fig. 3b). Moreover, the percentage of early apoptotic cell after PDT treatment was also increased. These results suggested that **1** is a good apoptosis inducer under irradiation [26].

Mitochondria play an essential role in the progression of apoptosis. Decreased mitochondrial membrane potential (MMP) has been implicated as an early event of apoptotic cells [25]. The change of MMP could be detected by the ratio of the red and green fluorescent intensity. As shown in Fig. 4a, in the control group, the ratio of red/green is 24.2; however in A549 cells exposed to 1.25/2.5 μM of **1** PDT treatment, the ratios are 13.68 and 6.09, respectively. The reduction of values suggested that **1** caused mitochondrial dysfunction. Furthermore, the reduction of MMP induced by corrole is concentration-dependent [45]. Mitochondrial membrane potential collapse is closely associated with the mitochondrial production of ROS [46]. To determine whether **1** induced the cell apoptosis by ROS, we evaluated the intracellular ROS generation in A549 cells [47, 48]. As shown in Fig. 4b, the DCF fluorescence intensity increased significantly when the A549 cells were exposed to **1** PDT treatment, and the fluorescence intensity also showed a concentration-dependent effect. Altogether, these results indicated that **1** induced A549 cell apoptosis through the mitochondrial pathway by inducing ROS production [26, 49].

The expression of apoptosis-related proteins in A549 cells was also measured. P53 plays a critical role in the execution of apoptosis, and concomitant PARP (poly ADP-ribose polymerase) cleavage occurs in a caspase-dependent manner [50]. The p53-dependent apoptosis and mitochondrial caspase apoptosis pathways are the most common models in the process of cell apoptosis [48]. Generally, the emergence of cleavage PARP protein is the marker of cell apoptosis [26, 51]. As shown in Fig. 5, after receiving **1** and illumination, the cleavage PARP (89 kb) appeared in the A549 cells; the increased expression of p53 was also found. The level of Bid was decreased; the activities of caspase-9 and caspase-3 were significantly

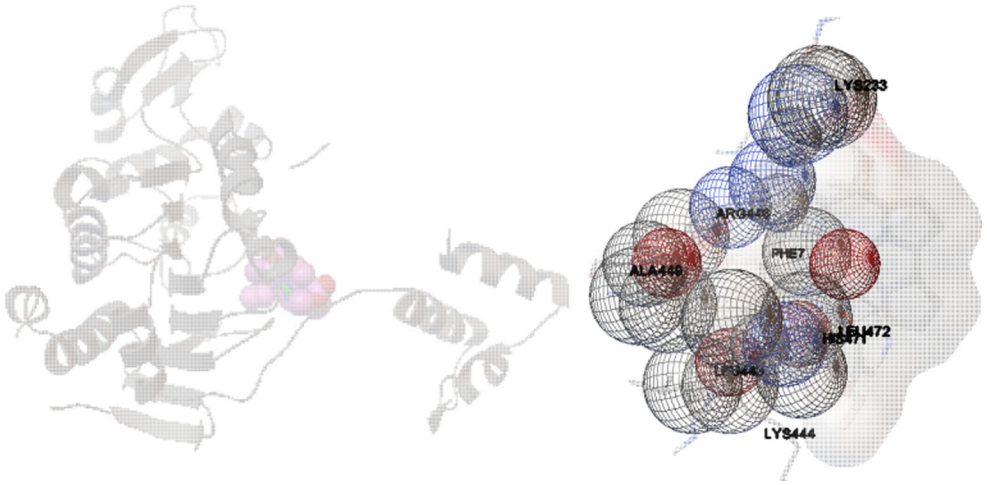

Fig. 7 Molecular docking simulation between **1** and SIRT1 protein

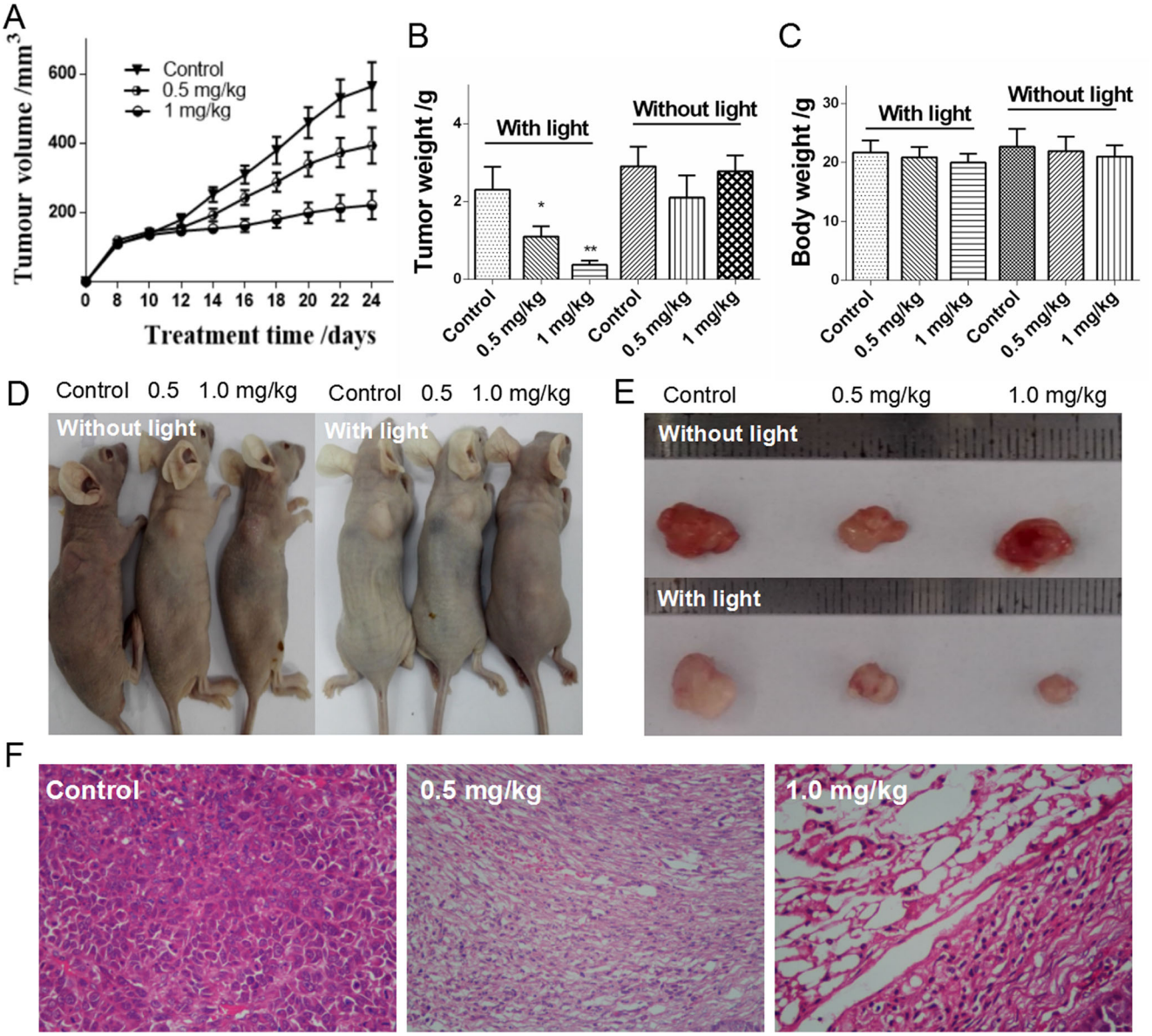

Fig. 8 The photodynamic anti-tumor effect of corrole **1** in A549 xenograft tumors. **a** The tumor volume from each group of mice at the end of the observation period. **b** The weight of the tumors for each group. **c** The body weight of mice from each group at the end of the observation period. Data are presented as the mean ± SEM. The images of euthanized mice and excised tumors from each group. Representative mice (**d**) and tumor (**e**) images at 24 days post-PDT treatment. **f** Histology analysis by H&E

enhanced, as indicated by their cleavage. Therefore, those results suggested that **1**'s phototoxicity could inhibit the growth of A549 cell by inducing apoptosis though activating the mitochondrial caspase apoptosis pathway [26, 52].

SIRT1, a member of histone deacetylase protein family, is widely expressed in various cells and helps tumor cell survival and growth [53, 54]. The expression level of anti-apoptotic protein [55, 56] SIRT1 was downregulated significantly in the PDT activity (Fig. 6), resulting in mitochondrial dysfunction, further to activate caspase apoptosis pathway [57, 58] (Fig. 9).

Furthermore, the potential anti-tumor effect of **1** in vivo was assessed in human tumor xenografts in mice. All of these data showed that **1** exhibited excellent anti-tumor ability in the inhibition of lung tumor growth. As a PS in photodynamic therapy, corrole has more potential for clinical application [26], the low dose/irradiation (0.5 mg/kg, 10-min irradiation and repeating only 2 days), and high toxicity (inhibitory rate 83.8%) comparing to porphyrin [59].

Conclusions

In summary, we can clearly found that cationic sulfonated corrole is a potential candidate of PS. The phototoxicity of **1** could induce A549 cell apoptosis by ROS production, further to activate the mitochondrial apoptosis pathway. We

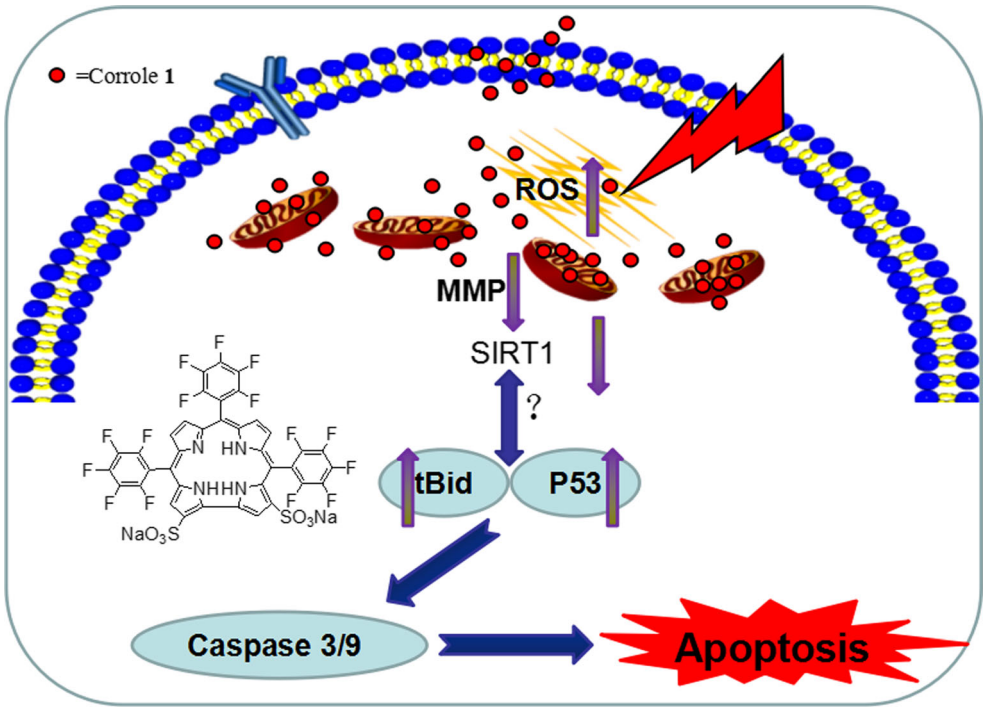

Fig. 9 Proposed signaling pathway of **1**'s photocytotoxity induced apoptosis in A549 cells under irradiation

concluded that SIRT1 protein is a more appropriate target in this progress. In vivo PDT test showed that **1** is a promising PS and worthy of further pre-clinical evaluation.

Funding This work is financially supported by National Natural Science Foundation of China (NNSFC) (Nos. 21671068, 81772634), Postdoctoral Initial Foundation of Guangdong Medical University (No. BH08073), Science Foundation of Guangdong Medical University (No. 2001/2XK16042), and Science Foundation of Zhanjiang (2017B01064).

Compliance with ethical standards

Conflict of interest The authors declare that they have no conflict of interest.

Ethical approval All procedures performed in studies involving animal participants were in accordance with the ethical standards of the institutional and/or national research committee. Animal experiments were performed in accordance with protocols approved by the institutional ethics committee of Guangdong Medical University (ID Number GDY1702014), and the detailed information can be found in the suggestion of animal research ethics.

Publisher's note Springer Nature remains neutral with regard to jurisdictional claims in published maps and institutional affiliations.

References

1. Paolesse R (2000) In: Kadish KM, Smith KM, Guilard R (eds) Porphyrin Handbook, Vol. 2. Academic Press, San Diego, pp 201–232
2. Liu HY, Lai TS, Yeung LL, Chang CK (2003) First synthesis of perfluorinated corrole and its Mn=O complex. Org Lett 5(5):617–620
3. Fu BQ, Huang J, Ren L, Weng XC, Zhou YY, Du YH, Wu XJ, Zhou X, Yang GF (2007) Cationic corrole derivatives: a new family of G-quadruplex inducing and stabilizing ligands. Chem Commun 0(31):3264–3266. https://doi.org/10.1039/B704599A
4. Mahammed A, Gross Z (2017) Corroles as triplet photosensitizers. Coord Chem Rev. https://doi.org/10.1016/j.ccr.2017.08.028
5. Fu BQ, Zhang D, Weng XC et al (2008) Cationic metal-corrole complexes: design, synthesis, and properties of guanine-quadruplex stabilizers. Chem Eur J 14(30):9431–9441
6. Zou HB, Yang H, Liu ZL et al (2015) Iron(IV)-corrole catalyzed stereoselective olefination of aldehydes with ethyl diazoacetate. Organometn 34(12):2791–2795
7. Preuß A, Saltsman I, Mahammed A et al (2014) Photodynamic inactivation of mold fungi spores by newly developed charged corroles. J Photochem Photobiol B 133(5):39–46
8. Okun Z, Kupershmidt L, Amit T et al (2009) Manganese corroles prevent intracellular nitration and subsequent death of insulin-producing cells. ACS Chem Biol 4(11):910–914
9. Haber A, Mahammed A, Fuhrman B et al (2008) Amphiphilic/bipolar metallocorroles that catalyze the decomposition of reactive oxygen and nitrogen species, rescue lipoproteins from oxidative damage, and attenuate atherosclerosis in mice. Angew Chem Int Ed 47(41):7896–7900
10. Teo RD, Hwang YY, Termini J, Gross Z, Gray HB (2017) Fighting cancer with corroles. Chem Rev 117(4):2711–2729
11. Gross Z, Mahammed A, Abdales M, Weaver JJ, Gray HB (2003) Bioinorganic chemistry of corrole metal complexes: interactions with proteins and cells. J Inorg Biochem 96(1):140
12. Lim P, Mahammed A, Okun Z et al (2012) Differential cytostatic and cytotoxic action of metallocorroles against human cancer cells: potential platforms for anticancer drug development. Chem Res Toxicol 25(2):400–409

13. Agadjanian H, Weaver JJ, Mahammed A et al (2006) Specific delivery of corroles to cells via noncovalent conjugates with viral proteins. Pharm Res 23(2):367–377
14. Agadjanian H, Ma J, Rentsendorj A et al (2009) Tumor detection and elimination by a targeted gallium corrole. PNAS 106(15): 6105–6110
15. Hwang JY, Lubow J, Chu D, Ma J, Agadjanian H et al (2011) A mechanistic study of tumor-targeted corrole toxicity. Mol Pharm 8(6):2233–2243
16. Aviv-Harel I, Gross Z (2011) Coordination chemistry of corroles with focus on main group elements. Coord Chem Rev 255(7–8): 717–736
17. Chang CK, Kong P, Liu HY et al (2006) Synthesis and photodynamic activities of modified corrole derivatives on nasopharyngeal carcinoma cells. Proc SPIE, SPIE: Bellingham WA USA 6139: 268–278. https://doi.org/10.1117/12.646328
18. Hwang JY, Lubow DJ, Chu D et al (2012) Photoexcitation of tumor-targeted corroles induces singlet oxygen-mediated augmentation of cytotoxicity. J Control Release 163(3):368–373
19. Sims JD, Hwang JY, Wagner S et al (2015) A corrole nanobiologic elicitstissue-activated MRI contrast enhancement and tumor-targeted toxicity. J Control Release 217(10):92–101
20. Barata JFB, Zamarrón A, Neves MGPMS et al (2015) Photodynamic effects induced by meso-tris(pentafluorophenyl)corrole and its cyclodextrin conjugates on cytoskeletal components of HeLa cells. Eur J Med Chem 92(6): 135–144
21. Liang ZH, Liu HY, Zhou R et al (2016) DNA-binding, photocleavage, and photodynamic anti-cancer activities of pyridyl corroles. J Membr Biol 249(4):419–428
22. Wang YG, Zhang Z, Wang H, Liu HY (2016) Phosphorus(V) corrole: DNA binding, photonuclease activity and cytotoxicity toward tumor cells. Bioorg Chem 67:57–63
23. Liang ZH, Liu HY, Jiang GB, Wen JY, Liu YJ, Xiao XY (2016) Polyhydric corrole and its gallium complex: synthesis, DNA-binding properties and photodynamic activities. Chin J Chem 34(10):997–1005
24. Shi L, Yang WC, Zeng SY et al (2016) DNA-binding and antitumor activities of cobalt corrole complexes. Chem J Chin Univ 37(6):1059–1068. https://doi.org/10.7503/cjcu20160029
25. Cheng F, Huang LT, Wang HH et al (2017) Photodynamic therapy activities of 10-(4-formylphenyl)-5,15-bis(pentafluorophenyl)corrole and its gallium complex. Chin J Chem 35(1):86–92
26. Zhang Z, Wang HH, Yu HJ et al (2017) Synthesis, characterization and in vitro and in vivo photodynamic activities of a gallium(III) tris(ethoxycarbonyl)corrole. Dalton Trans 46(29):9481–9490
27. Zhang Z, Wen JY, Lv BB et al (2016) Photocytotoxicity and G-quadruplex DNA interaction of water-soluble gallium(III) tris (N-methyl-4-pyridyl)corrole complex. Appl Organomet Chem 30(3): 132–139
28. Zhang Y, Wen JY, Wang XL et al (2014) DNA binding and nuclease activity of cationic iron(IV) and manganese(III) corrole complexes. Appl Organomet Chem 28(7):559–566
29. Na N, Zhao DQ, Li H, Jiang N, Wen JY, Liu HY (2016) DNA binding, photonuclease activity and human serum albumin interaction of a water-soluble freebase carboxyl corrole. Molecules 21(1): 1–14. https://doi.org/10.3390/molecules21010054
30. Zhang Y, Wang Q, Wen JY et al (2013) DNA binding and oxidative cleavage by a water-soluble carboxyl manganese(III) corrole. Chin J Chem 31(10):1321–1328
31. Lu J, Liu HY, Shi L et al (2011) DNA cleavage mediated by water-soluble manganese corrole. Chin Chem Lett 22(1):101–104
32. Zhang Y, Wen JY, Mahmood MHR, Wang XL, Lv BB, Ying X, Wang H, Ji LN, Liu HY (2015) DNA/HSA interaction and nuclease activity of an iron(III) amphiphilic sulfonated corrole. Luminescence 30(7):1045–1054
33. Huang JT, Wang XL, Zhang Y et al (2013) DNA binding and nuclease activity of a water-soluble sulfonated manganese(III) corrole. Transit Met Chem 38(3):283–289
34. Zhang HT, Wu J, Wen M, Su LJ, Luo H (2012) Galangin induces apoptosis in hepatocellular carcinoma cells through the caspase 8/t-bid mitochondrial pathway. J Asian Nat Prod Res 14(7):626–633
35. Zhang HT, Li N, Wu J, Su LJ, Chen XY, Lin BY, Luo H (2013) Galangin inhibits proliferation of HepG2 cells by activating AMPK via increasing the AMP/TAN ratio in a LKB1-independent manner. Eur J Pharmacol 718(1–3):235–244
36. Lucky SS, Soo KC, Zhang Y (2015) Nanoparticles in photodynamic therapy. Chem Rev 115(4):1990–2042
37. Ethirajan M, Chen YH, Joshi P, Pandey RK (2011) The role of porphyrin chemistry in tumor imaging and photodynamic therapy. Chem Soc Rev 40(1):340–362
38. Calixto GMF, Bernegossi J, Freitas LM, Fontana CR, Chorilli M (2016) Nanotechnology-based drug delivery systems for photodynamic therapy of cancer: a review. Molecules 21(3):342
39. Jeon S, Wang M, Tan LS, Cooper T, Hamblin MR, Chiang LY (2013) Synthesis of photoresponsive dual NIR two-photon absorptive [60]fullerene triads and tetrads. Molecules 18(8):9603–9622
40. Xia CH, Wang Y, Chen W, Yu WX, Wang BQ, Li T (2011) New hydrophilic /lipophilic tetra-α-(4-carboxyphenoxy) phthalocyanine zinc-mediated photodynamic therapy inhibits the proliferation of human hepatocellular carcinoma Bel-7402 cells by triggering apoptosis and arresting cell cycle. Molecules 16(2):1389–1401
41. Simone BCD, Mazzone G, Russo N, Sicilia E, Toscano M (2017) Metal atom effect on the photophysical properties of Mg(II), Zn(II), Cd(II), and Pd(II) tetraphenylporphyrin complexes proposed as possible drugs in photodynamic therapy. Molecules 22(7):1093
42. Rodriguez ME, Zhang P, Azizuddin K et al (2009) Structural factors and mechanisms underlying the improved photodynamic cell killing with silicon phthalocyanine photosensitizers directed to lysosomes versus mitochondria. Photochem Photobiol 85(5):1189–1200
43. Wang H, Zheng JH, Xu WJ et al (2017) A new series of cytotoxic pyrazoline derivatives as potential anticancer agents that induce cell cycle arrest and apoptosis. Molecules 22(10):1635
44. Miniotis MF, Mukwaya A, Wingren AG (2014) Digital holographic microscopy for non-invasive monitoring of cell cycle arrest in L929 cells. PLoS One 9(9):e106546
45. Meschini S, Pellegrini E, Condello M, Occhionero G, Delfine S, Condello G, Mastrodonato F (2017) Cytotoxic and apoptotic activities of prunus spinosa trigno ecotype extract on human cancer cells. Molecules 22(10):157. https://doi.org/10.3390/molecules22091578
46. Rasul A, Bao R, Malhi M, Zhao B, Tsuji I, Li J, Li XM (2013) Induction of apoptosis by costunolide in bladder cancer cells is mediated through ROS generation and mitochondrial dysfunction. Molecules 18(2):1418–1433
47. Kankala RK, Tsai PY, Kuthati Y, Wei PR, Liu CL, Lee CH (2017) Overcoming multidrug resistance through co-delivery of ROS-generating nano-machinery in cancer therapeutics. J Mater Chem B 5(7):1507–1517
48. Kankala RK, Kuthati Y, Liu CL, Lee CH (2015) Hierarchical coated metal hydroxide nanoconstructs as potential controlled release carriers of photosensitizer for skin melanoma. RSC Adv 5(53): 42666–42680
49. Kankala RK, Liu CG, Chen AZ et al (2017) Overcoming multidrug resistance through the synergistic effects of hierarchical pH-sensitive, ROS-generating nanoreactors. ACS Biomater-SCI Eng 3(10): 2431–2442
50. Shukla S, Sharma A, Pandey VK, Raisuddin S, Kakkar P (2016) Concurrent acetylation of FoxO1/3a and p53 due to sirtuins inhibition elicit Bim/PUMA mediated mitochondrial dysfunction and

apoptosis in berberine-treated HepG2 cells. Toxicol Appl Pharmacol 291(15):70–83
51. Suzuki M, Bandoski C, Bartlett JD (2015) Fluoride induces oxidative damage and SIRT1/autophagy through ROS-mediated JNK signaling. Free Radic Biol Med 89:369–378
52. Kessel D, Vicente MGH, Jr JJR (2006) Initiation of apoptosis and autophagy by photodynamic therapy. Lasers Surg Med 38(5):482–488
53. Li X, Wang YJ, Xiong YZ, Wu J, Ding H, Chen XY, Lan LB, Zhang HT (2016) Galangin induces autophagy via deacetylation of LC3 by SIRT1 in HepG2 cells. Sci Report 07(6):30496
54. Oberdoerffer P, Michan S, Mcvay M et al (2008) SIRT1 redistribution on chromatin promotes genomic stability but alters gene expression during aging. Cell 135(5):907–918
55. Panta K, Yadava AK, Guptaa P, Islama R, Sarayab A, Venugopal SK (2017) Butyrate induces ROS-mediated apoptosis by modulating miR-22/SIRT-1 pathway in hepatic cancer cells. Redox Biol 12:340–349
56. Reiners JJ Jr, Caruso JA, Mathieu P, Chelladurai B, Yin XM, Kessel D (2002) Release of cytochrome c and activation of pro-caspase-9 following lysosomal photodamage involves bid cleavage. Cell Death Differ 9(9):934–944
57. Kessel D, Jr JJR (2017) Effects of combined lysosomal and mitochondrial photodamage in a non-small-cell lung cancer cell line: the role of paraptosis. Photochem Photobiol 93(6):1502–1508
58. Whitacre CM, Satoh TH, Xue LY, Gordon NH, Oleinick NL (2002) Photodynamic therapy of human breast cancer xenografts lacking caspase-3. Cancer Lett 179(1):43–49
59. Idris NM, Gnanasammandhan MK, Zhang J, Ho PC, Mahendran R, Zhang Y (2012) In vivo photodynamic therapy using upconversion nanoparticles as remote-controlled nanotransducers. Nat Med 18(10):1580–1585